

An Effective Morphology Control of Hydroxyapatite Crystals via Hydrothermal Synthesis

Inés S. Neira,^{*,†,‡,§} Yury V. Kolen'ko,^{‡,||} Oleg I. Lebedev,[#] Gustaaf Van Tendeloo,[#] Himadri S. Gupta,[§] Francisco Guitián,[†] and Masahiro Yoshimura[‡]

Galician Institute of Ceramics, University of Santiago de Compostela, E-15782 Santiago de Compostela, Spain, Materials and Structures Laboratory, Tokyo Institute of Technology, 4259 Nagatsuta, Midori-ku, 226-8503 Yokohama, Japan, Department of Biomaterials, Max Planck Institute of Colloids and Interfaces, D-14424 Potsdam, Germany, and Electron Microscopy for Materials Science, University of Antwerp, B-2020 Antwerp, Belgium

Received July 9, 2008; Revised Manuscript Received September 8, 2008

ABSTRACT: A facile urea-assisted hydrothermal synthesis and systematic characterization of hydroxyapatite (HA) with calcium nitrate tetrahydrate and diammonium hydrogen phosphate as precursors are reported. The advantage of the proposed technique over previously reported synthetic approaches is the simple but precise control of the HA crystals morphology, which is achieved by employing an intensive, stepwise, and slow thermal decomposition of urea as well as varying initial concentrations of starting reagents. Whereas the plate-, hexagonal prism- and needle-like HA particles preferentially growth along the *c*-axis, the smaller and fine-plate-like HA crystals demonstrate crystal growth along the (102) and (211) directions, uncommon for HA. Furthermore, it was established that the hydrothermally derived powdered products are phase-pure HA containing CO₃²⁻ anions in the crystal lattice, that is, AB-type carbonated hydroxyapatite. Transmission electron microscopy (TEM) and electron diffraction (ED) of selected samples reveal that the as-prepared HA crystals are single-crystalline and exhibit a nearly defect-free microstructure. The hardness and elastic modulus of the hexagonal prism-like HA crystals have been investigated on a nanoscale using the nanoindentation technique; the observed trends are discussed.

Introduction

In recent years, hydroxyapatite Ca₁₀(PO₄)₆(OH)₂ (HA) has attracted great interest in modern materials chemistry because of its high potential for progressing chromatography¹ and, especially, biomaterials.² Specifically, owing to the intrinsically different surface reactivity—positively charged calcium-rich *c*-surface and negatively charged hydroxyl- and phosphate-rich *a*-surface (see Supporting Information, Figures S1 and S2)—HA exhibits selective adsorption of various ions, organic compounds, and proteins,¹ and therefore becomes an important material for chromatographic uses. Another and one of the most appealing features of HA is that it exhibits excellent biocompatibility and bioactivity, which make HA and related biomaterials a key constituent class of compounds for the biomedical applications.²

For these peculiar physical-chemical and biological-physiological properties, the material properties such as particle size, dimensional anisotropy, morphology, real microstructure, etc. are of critical importance for optimization and applications. For example, plate-like and fibrous HA particles exhibit enhanced adsorption properties because of their charging surface efficiency.^{3,4} Crystals with plate-like morphology are also the most effective to stiffen isotropic composite materials, followed by the fibrous shaped one; the least effective geometry is the spherical one.⁵ In this way, HA crystals with dedicated morphological features are capable for moderated reinforcement of the biomaterials for bone repair and substitution, such as

calcium phosphate bone-cements, biocomposites, etc.^{6,7} In addition, carbonated HA is the main inorganic component in calcified hard tissues of vertebrates, present in human bones and tooth enamel in the form of platelet-like nanocrystals and polycrystalline hexagonal prisms, respectively.^{8,9} Nevertheless, as a result of functional irregularities, vertebrates can generate HA pathologically (i.e., ectopic calcification), resulting in the formation of renal and bile stones, calcifications of cartilages, basal ganglia, etc.¹⁰ Hence, synthetic HA crystals with specific morphological and structural properties can provide a unique tool to approach the understanding of these inappropriate biomineralization phenomena.¹¹

The preparation of phase-pure, well-defined HA crystals with controlled morphology has been the focus of intensive research over the last decades.¹² Several approaches have been realized. The main methods include growth in a gel system,¹³ molten salts synthesis,¹⁴ liquid–solid-solution synthesis,¹⁵ electrochemical deposition,¹⁶ hydrolysis,¹⁷ and mainly the hydrothermal route.¹⁸ The latter is a most promising and convenient way because of its successful application for a one-pot synthesis of a desired phase under gentle reaction conditions.¹⁸ Remarkably, the hydrothermal technique is also well-known as an efficient approach to synthesize defect-free single crystals of high crystallinity with a relatively narrow particle size distribution and distinct morphological features.¹⁹

We have previously synthesized HA whiskers via a low-temperature hydrothermal method.²⁰ This synthesis procedure takes advantage of the fact that the gradual increase of pH induces an advanced hydrothermal crystal growth, thus generating a large quantity of HA particles in the form of sharply faceted hexagonal prisms. In this paper, we present a modification of this synthesis route that allows us to obtain phase-pure hydroxyapatite single crystals with a controlled morphology. In particular, we detail here a template-free synthesis of well-defined *plate-like*, *hexagonal prism-like*, *needle-like*, and *fine-*

* Corresponding author. Mail: Inés Sánchez Neira, Instituto de Cerámica de Galicia, Universidade de Santiago de Compostela, Avda. Mestre Mateo, s/n, E-15782 Santiago de Compostela, Spain. Phone: +34-981-563-100, ext. 16885. Fax: +34-981-564-242. E-mail: ines.sanchez@usc.es.

[†] University of Santiago de Compostela.

[‡] Tokyo Institute of Technology.

[§] Max Planck Institute of Colloids and Interfaces.

^{||} Present address: Department of Inorganic Chemistry, Fritz Haber Institute of the Max Planck Society, D-14195 Berlin, Germany.

[#] University of Antwerp.

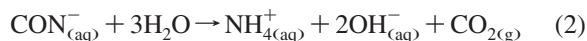
Table 1. Summary of Synthesis Conditions and Results of Selected Hydrothermal Reactions

sample	concentration, M			applied temperature profile	pH _{final}	XRD phase composition	SEM particles morphology
	[Ca ²⁺]	[PO ₄ ³⁻]	[urea]				
PT	0.1670	0.10	0.50	Scheme I	8.5	HA	plates
HX	0.1670	0.10	0.50	Scheme II	8.1	HA	hexagonal prisms
ND	0.1670	0.10	0.50	Scheme III	8.4	HA	needles
FP	0.0835	0.05	0.25	Scheme IV	8.4	HA	fine-plates

plate-like HA crystals through a simple variation of the hydrothermal treatment parameters. Nanoindentation probing of the mechanical properties of the as-synthesized hexagonal prism-like HA single crystals is also presented. The obtained results are compared with reported data, thus enabling a discussion of the structure–property relationship in conjunction with the influence of the preparation method on the properties. The proposed synthesis approach requires only low-cost reagents, reducing the cost of the synthesis of HA crystals with different morphologies, and making it attractive for potential applications.

Experimental Section

Synthesis. Hydroxyapatite crystals with different morphology were synthesized via a direct hydrothermal reaction between calcium nitrate tetrahydrate (Ca(NO₃)₂·4H₂O, 98.5% Wako) and diammonium hydrogen phosphate ((NH₄)₂HPO₄, 99.0% Wako) using urea ((NH₂)₂CO, 99.0% Wako) as a homogeneous precipitation agent. At elevated temperatures, (NH₂)₂CO continuously decomposes to form carbon dioxide and aqueous ammonia species according to the eqs 1 and 2:



In turn, such in situ released NH₃(aq) generates a gradual increase of the reaction solution pH to the values wherein HA becomes the more thermodynamically stable calcium orthophosphate compound (i.e., less-soluble), and is thus formed.²¹ The main advantage of the urea-assisted approach is that urea hydrolyzed homogeneously—if the reaction medium is uniform with respect to concentration and temperature—thereby generating the driving force toward the nucleation and growth of HA crystals under moderated supersaturation conditions.

The synthesis proceeds by mixing stoichiometric amounts of Ca(NO₃)₂·4H₂O and (NH₄)₂HPO₄ (Ca/P molar of 1.67) together with an appropriate amount of urea in 25 mL of distilled water under vigorous stirring in a 40 mL poly(tetrafluoroethylene) (PTFE) vessel (Table 1). The suspension pH was then adjusted to ~3 by 0.5 M nitric acid aqueous solution (HNO₃, 63% Wako) using a Mettler Toledo InLab413 SG pH meter, and the resulting mixture was stirred for a further 15 min. Afterward, the pH was subsequently readjusted to 3.00 ± 0.05 under constant stirring and the solution volume was filled to 35 mL with distilled water. The vessel was capped by a PTFE cover and placed into a stainless steel autoclave. The autoclave was sealed and subjected to the heat treatment (*T*_{max} = 90 °C).

All our attempts to use a completely closed hydrothermal reaction system for the synthesis of the title compound were unsuccessful due to the eventually high autogenous pressure of CO₂, which is additionally poorly soluble in water under elevated temperatures, thereby suppressing the driving force for urea decomposition. This drawback was successfully overcome by using a 1.5-mm-thick, low-density (0.6 g/cm³) HYPER-SHEET gasket (GORE-TEX) with a porous structure of PTFE polymer (see Supporting Information, Figure S3). Such a gasket is semipermeable to gaseous products under elevated temperatures, thus enabling a gradual release of the CO₂ forming during the urea temperature decomposition.^{20,22}

Since the decomposition of (NH₂)₂CO is a thermally induced, temperature-dependent process,²³ we tried to govern its decomposition rate, and accordingly the saturation of the reaction solution, using four different temperature profiles in the course of the hydrothermal treatment. In this way, intensive, stepwise, slow, and interrupted thermal decomposition of urea can be achieved by applying Schemes I, II, III, and IV, respectively (Table 1, Figure 1).

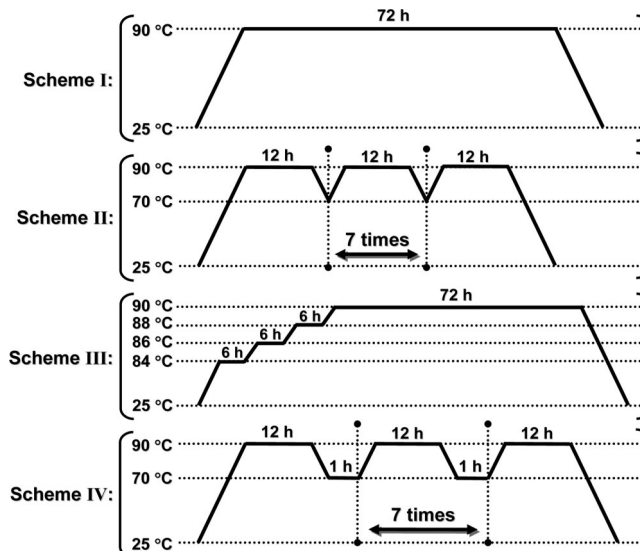


Figure 1. Schematic representations (Schemes I–IV) of controlled temperature profiles applied during the hydrothermal treatments. Heating or cooling rates of 0.5 °C/min were used.

The products of the hydrothermal synthesis were obtained in two forms: an abundant cotton-like suspension and secondary wall-product firmly attached to the PTFE vessel's walls (see Supporting Information, Figure S4). Both crystalline materials were carefully separated, collected by filtration, washed with distilled water and ethanol, and finally dried at 80 °C. Taking into account the overwhelming yield of the products recovered from the cotton-like suspension as well as their fine homogeneity, the research described below is devoted only to these samples.

Throughout this work, a set of acronyms is used (Table 1), wherein the first two letters mean the obtained sample morphology in form of plates (**PT**), hexagonal prisms (**HX**), needles (**ND**), and fine-plates (**FP**).

Characterization. The products were characterized by powder X-ray diffraction (XRD) using a Rigaku RINT 2000 diffractometer with Ni-filtered CuK_α radiation (λ = 1.54178 Å), operating at 200 mA and 50 kV. The phases were identified by comparison with the data reported in the Joint Committee of Powder Diffraction Standards (JCPDS) database. The room temperature diffuse reflectance infrared (IR) Fourier-transform spectra were recorded on a Jeol JIR-7000 spectrometer with a resolution of 4 cm⁻¹ and a number of scans 100. The carbon content was quantitatively determined by combustion bulk elemental analysis using a Fisons EA 1108 elemental analyzer. The room temperature Raman scattering measurements were carried out on a confocal Raman microscope WITEC CRM200 with linear polarized laser light (λ = 532 nm) as the excitation source. Energy-dispersive X-ray spectroscopy investigations (EDX) for semiquantitative Ca and P content determination were performed with a EDAX DX-95 spectrometry system. The morphology was studied by scanning electron microscopy (SEM) and field-emission environmental SEM (FE-ESEM) using Hitachi S-4500 and FEI Quanta 600F microscopes operating at 15 and 5 kV, respectively. Transmission electron microscopy (TEM), electron diffraction (ED) and high-resolution TEM (HRTEM) investigations were performed using a Jeol 4000EX microscope operating at 400 kV and having 0.17 nm point resolution. The samples for TEM were crushed in methanol and deposited on a holey carbon grid.

The elastic modulus (*E*_s, related to elastic deformations) and hardness (*H*, related to plastic deformations) of HA single crystals with a well-defined hexagonal prism-like morphology were estimated by the

nanindentation technique (NI). For this purpose, the HA particles were embedded in an advanced calcium phosphate bone-cement, recently developed by us. NI experiments were performed on a Hysitron TriboScan UBI-1 nanohardness tester in conjunction with a Digital Instruments Nanoscope III atomic force microscope (AFM), and both the prism-faceted (i.e., *a*-surface exposed) and basal-faceted (i.e., *c*-surface exposed) planes of HA crystals were probed. A Berkovich diamond indenter tip with a regular triangle pyramid geometry and a nominal radius of 300 nm was used. The reduced indentation modulus (E_r) and H were calculated from the load-displacement data obtained by NI using the method of Oliver and Pharr.²⁴ E_r is related to E_s of the test sample through the eq 3:

$$\frac{1}{E_r} = \frac{(1 - \nu_i^2)}{E_i} + \frac{(1 - \nu_s^2)}{E_s} \quad (3)$$

where ν_i is the Poisson's ratio for the diamond tip (0.07),²⁵ ν_s is the Poisson's ratio for synthetic HA (0.28),²⁶ and E_i is the diamond elastic modulus (1141 GPa).²⁵ In the current study, a loading function with a peak load of 1 mN, loading rate of 0.2 mN/s, holding time 60 s, unloading to 0.05 mN with rate of 0.2 mN/s, holding at 0.05 mN for 20 s and unloading back to 0 mN with rate of 0.5 mN/s was used. Both E_s and H values are the average of at least 30 probeings. A detailed description of the sample preparation for NI and respective data analysis is presented in the Supporting Information.

Results

Synthesis. Hydroxyapatite crystals with different morphological features were prepared by the direct reaction between $\text{Ca}(\text{NO}_3)_2 \cdot 4\text{H}_2\text{O}$ and $(\text{NH}_4)_2\text{HPO}_4$ under gentle hydrothermal conditions ($T_{\text{max}} = 90^\circ\text{C}$). The initial concentrations of starting reagents, post-synthesis reaction solution pH, phase composition and overall particles morphology of the hydrothermally derived products are given in Table 1; four applied temperature regimes are presented in Figure 1. The starting solution pH was fixed at an optimal value of 3.²⁰ Phase-pure powders can be prepared readily on a gram scale under the listed conditions (Table 1). Hydrothermal syntheses using either higher concentrations of the reactants or 1.5 times higher/lower concentrations of urea were ineffective and did not result in the formation of phase-pure HA.

XRD. The powder XRD patterns of the synthesized samples are presented in Figure 2A, indicating an overall crystalline nature of the products. According to the phase analysis, samples **PT**, **HX**, **ND**, and **FP** are phase-pure hydroxyapatite $\text{Ca}_{10}(\text{PO}_4)_6(\text{OH})_2$ (JCPDS No. 72-1243, hexagonal, $a = 9.4320 \text{ \AA}$, $c = 6.8810 \text{ \AA}$, space group $P6_3/m$). Whereas the XRD pattern of the **FP** powder closely resembles the diffraction peaks reported in the JCPDS database, the ones from the **PT**, **HX**, and **ND** products are very similar to each other and clearly exhibit inconsistencies in the intensity of the Bragg reflections reported in the JCPDS database (Figure 2B). The latter observation most likely corresponds to the shape anisotropy (i.e., textured microstructure) of the particles in the as-synthesized products, indicating that the crystals in these samples grow along the *c*-axis (Figure 2B, inset); this is confirmed by TEM (vide infra). In turn, such crystal growth develops the *a*-plane of the hexagonal HA (see Supporting Information, Figure S2B); hence, the observed (300) XRD reflection representing *a*-plane growth is more intense than the one reported in the JCPDS database (Figure 2B).

IR. Figure 3A displays the IR spectra collected from the hydrothermal synthesis products. The set of bands and spectra features agrees fairly well with the reported IR data for phase-pure hydroxyapatite.²⁷ A set of characteristic bands representing apatitic PO_4^{3-} groups is observed at ~ 1104 , 1064 , and 1028 cm^{-1} (ν_3 triply degenerated asymmetric stretching mode of the

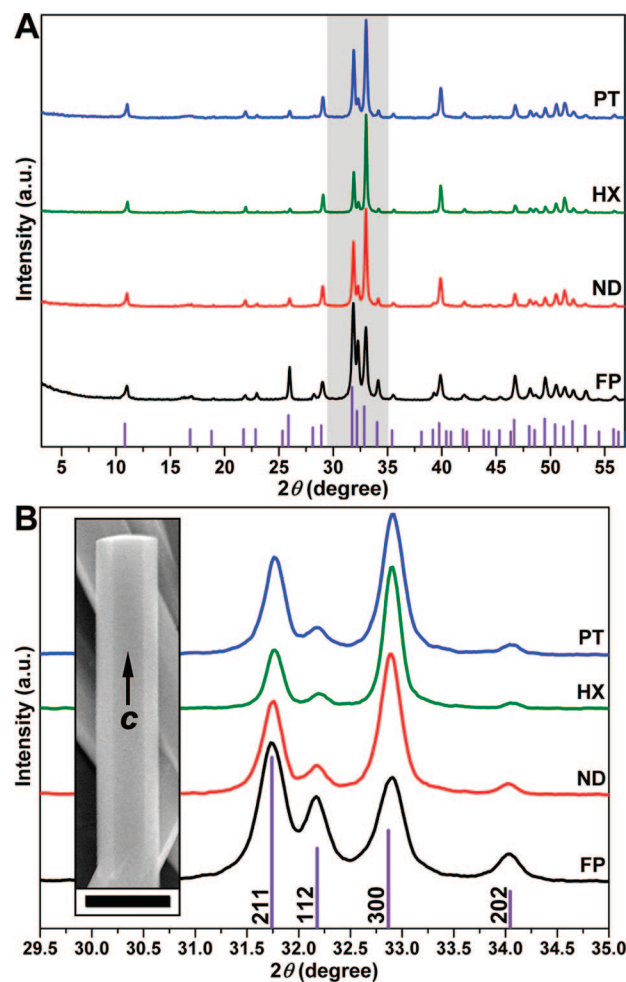


Figure 2. (A) XRD patterns from the hydrothermally derived **PT**, **HX**, **ND**, and **FP** samples. Tick marks below the patterns correspond to the positions of the Bragg reflections expected for the hexagonal HA (JCPDS No. 72-1243). (B) Enlargement of the angular region from $29.5^\circ < 2\theta < 35.0^\circ$ (marked by the gray region in (A)) where the (211), (112), (300), and (202) peaks of the HA phase are expected to be. In the inset a SEM image of an HA crystal exhibiting shape anisotropy and crystal growth along the *c*-axis is displayed (scale bar $5 \mu\text{m}$).

P—O bond) and $\sim 960 \text{ cm}^{-1}$ (ν_1 symmetric stretching mode of the P—O bond). Additional expected bands representing a ν_4 triply degenerated bending mode of the O—P—O bond (~ 604 , 578 , and 563 cm^{-1}) are also observed in the low wavenumber region.²⁷ The intense peak at $\sim 3570 \text{ cm}^{-1}$ and the weak one at $\sim 632 \text{ cm}^{-1}$ are assigned to the stretching (ν_s) and librational modes (ν_l) of the structural hydroxyl anions, respectively.²⁷ Moreover, their harmonic overtones and/or combination bands are also observed in the region between 2171 and 1923 cm^{-1} .²⁷ The broad weak peak at $\sim 3327 \text{ cm}^{-1}$ (distinct for **ND** and **FP** samples) is assigned to the physisorbed water.²⁸ Peaks observed in the 2400 – 2287 cm^{-1} range correspond to the atmospheric $\text{CO}_{2(\text{g})}$.²⁸ Inspection of the 1630 – 1194 cm^{-1} region clearly shows the existence of distinctive bands attributed to the carbonate groups (Figure 3A),²⁷ indicating their incorporation into the crystal structure of HA. In particular, the peaks observed at ~ 1544 and 879 cm^{-1} represent CO_3^{2-} anions partially occupying OH^- positions (A-type), while the bands detected at ~ 1451 , 1420 , and 874 cm^{-1} reflect partial PO_4^{3-} substitution (B-type).²⁹ Hence, all four hydrothermally derived samples are AB-type carbonated hydroxyapatite. These carbonate anions are believed to arise from the urea decomposition. This fact is very

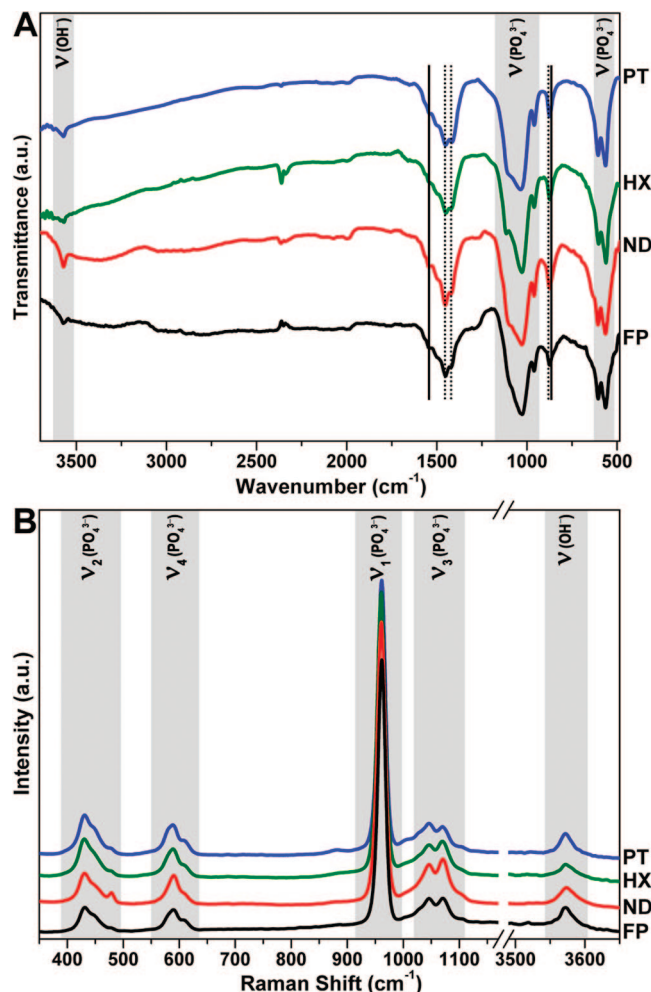


Figure 3. Comparison of IR (A) and Raman scattering (B) data for the hydrothermally derived **PT**, **HX**, **ND**, and **FP** powdered products. The characteristic stretching modes attributed to the apatitic phosphate PO_4^{3-} and hydroxyl OH^- groups are marked by gray regions. Solid and dotted lines are drawn in (A) at the positions of CO_3^{2-} anion vibrations to indicate A-type (carbonate replacing hydroxyl) and B-type (carbonate replacing phosphate) of carbonated HA, respectively.

consistent with the representative combustion bulk elemental analysis, which demonstrates that the **PT**, **HX**, **ND**, and **FP** samples contain approximately 0.61, 0.90, 0.70, and 0.80 wt% (weight percentage) of carbon, respectively.

Raman Scattering. Figure 3B shows the Raman scattering spectra from the powdered **PT**, **HX**, **ND**, and **FP** samples. The band positions for the hydrothermally derived HA phases are in good agreement with published data on bulk hydroxyapatite powder.²⁷ The spectra show a very intense characteristic peak at $\sim 969\text{ cm}^{-1}$ owing to the symmetric stretching mode $\nu_1(\text{PO}_4^{3-})$. Apart from this ν_1 mode, the other stretching modes of the PO_4^{3-} groups are also observed, namely, ν_2 in the $502\text{--}391\text{ cm}^{-1}$ region, ν_4 in the $646\text{--}559\text{ cm}^{-1}$ region, and ν_3 in the $1002\text{--}1110\text{ cm}^{-1}$ region.²⁷ The band at $\sim 3576\text{ cm}^{-1}$ corresponds to the stretching vibration of the hydroxyl groups.²⁷

EDX. The semiquantitative calcium and phosphorus content in the prepared samples was determined by EDX. The average molar ratios of the Ca to P elements (Ca/P) are ~ 1.76 , 1.74 , 1.75 , and 1.76 for the **PT**, **HX**, **ND**, and **FP** samples, respectively. Slightly higher Ca/P ratio values obtained for the hydrothermal products in comparison with stoichiometric HA (Ca/P = 1.67) could be ascribed to the partial substitution of

PO_4^{3-} and OH^- groups in the HA lattice by CO_3^{2-} anions, in agreement with IR and bulk elemental analyses.

SEM. Overall morphology of the synthesized HA powders, observed by SEM measurements, are listed in Table 1 and are also shown in Figure 4. The **PT** sample mostly consists of particles with a plate-like morphology exhibiting a nonuniform size distribution (Figure 4A). Crystal sizes in the as-prepared powder range from a few micrometers to a few tenths of a micrometer. The hydrothermal synthesis applying the temperature profile of Scheme II (Table 1, Figure 1) leads to a distinctly different morphology. SEM observations of the **HX** sample reveal an overwhelming quantity of elongated micrometer-sized particles with a sharp faceted hexagonal prism-like morphology. The crystals exhibit a relatively uniform size distribution: a width of about $1.5\text{--}2.1\text{ }\mu\text{m}$ and a length in the range from 9.5 to $15.5\text{ }\mu\text{m}$ (Figure 4B). Using the same synthesis route but applying the temperature regime of Scheme III, continuous crystals with a needle-like shape can be synthesized (Figure 4C). The as-prepared **ND** particles exhibit a nonuniform size distribution with sizes ranging from several tenths of a micrometer to a few hundreds of a micrometer. In sharp contrast to the these **PT**, **HX**, and **ND** products, synthesis using only half of the amount of Ca and P precursors as well as applying the temperature profile of Scheme IV (Figure 1) generates HA crystals exhibiting considerable smaller sizes with a less defined microstructure (Figure 4D). According to this SEM analysis, **FP** powder mostly consists of crystals exhibiting a fine-plate-like (predominant) and a rod-like particle morphology with typical sizes in the range from a few hundreds of a nanometer to a few micrometers.

TEM. The main panel in Figure 5A shows a representative low-magnification TEM image of a selected elongated particle of the **HX** sample. The sample mostly consists of elongated micrometer-sized particles, consistent with the SEM observations (Figure 4B). The corresponding $[010]^*$ ED pattern (top right inset in Figure 5A) can be completely indexed with reference to the hexagonal $P6_3/m$ space group, using the HA phase unit cell parameters of JCPDS No. 21-1272. From the orientation relation between image and diffraction, we conclude that the **HX** particles are exclusively oriented with their long axis along $[001]^*$, indicating a c -axis growth; consistent with the texturing effect observed by XRD (Figure 2B). All reflections in the ED pattern are very sharp, an indication of the perfection of the as-prepared HA crystals. A representative HRTEM image along the $[010]$ zone axis is given as the bottom inset in Figure 5A, confirming the perfect hydroxyapatite structure of the **HX** sample.

In contrast to the **HX** sample, TEM shows the presence of two different types of crystallized particles in the hydrothermally derived **FP** product (Figure 5B,C, main panels): thin, long rod-like and nearly rectangular predominant plate-like crystals. According to the ED analysis (Figure 5B,C, right top), both these morphologies are phase-pure HA particles possessing different growth directions; the rods exhibit $[221]$ orientation, while the plates are $[110]$ oriented, growing along the (102) and (211) direction, respectively. ED also reveals the single-crystalline nature and the structural perfection of these characteristic HA structures of **FP**. The right bottom inset in Figure 5B displays a representative HRTEM image from an HA single crystal along the $[221]$ zone axis. Close inspection of individual crystals on a large scale reveals the absence of any type of structural defects throughout the particles.

NI. The mechanical properties of phase-pure, structurally nearly perfect HA single crystals with a well-defined hexagonal

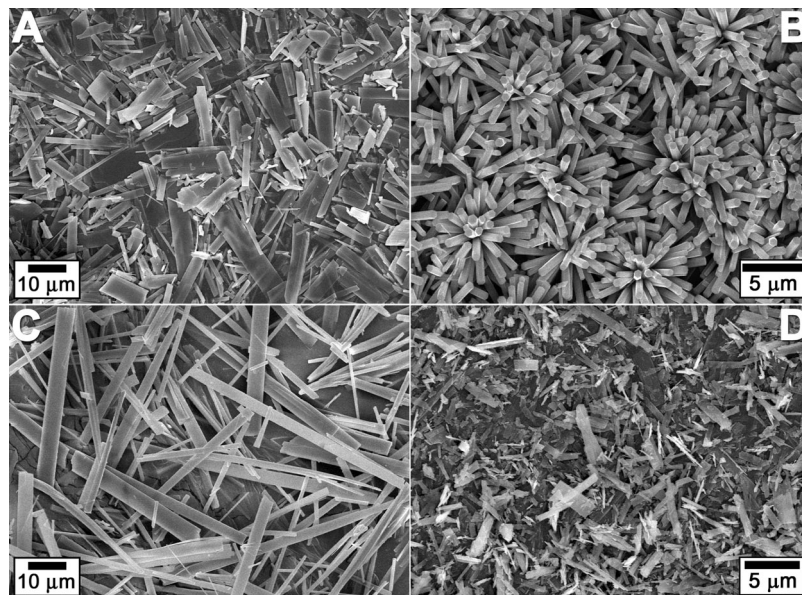


Figure 4. Comparison of the morphological features of hydrothermally derived products as imaged by SEM from **PT** (A), **HX** (B), **ND** (C), and **FP** (D) samples.

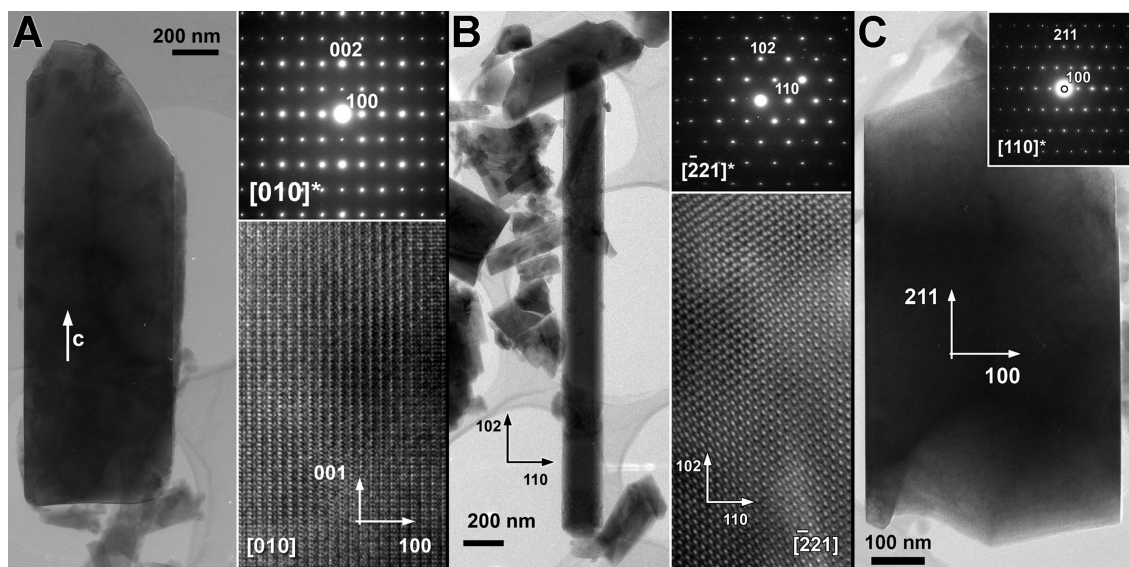


Figure 5. A low-magnification TEM images (main panels) together with the corresponding ED patterns (top right insets) and HRTEM images (bottom right insets). Note the typical growth direction of the HA crystals: along (001) in sample **HX** (A) and along (102) and (211) in sample **FP** (B, C).

prism-like morphology (sample **HX**) were studied using nanoindentation. Two representative load versus displacement curves collected on both prism- and basal-faceted crystal planes are shown in Figure 6A. These load-displacement profiles smoothly follow the loading function without any discontinuities or pop-in marks, confirming that no cracks arise during NI measurements.³⁰ According to the displacement profiles, a peak load of 1 mN generates residual indentation depths in the 15–20 nm range. The elastic module E_s and hardness H values of the HA single crystals were calculated to be about 62 ± 7 GPa and 5.9 ± 0.8 GPa for the prism-faceted plane and 68 ± 8 GPa and 5.7 ± 0.9 GPa for the basal-faceted plane, respectively. These calculated hardness values are not statistically significant different (Mann–Whitney rank sum test ($P = 0.359$)).

The inset in Figure 6A shows a representative FE-ESEM image of the surface of a nearly regular in shape basal-faceted

HA crystal after nanoindentation. The NI probing results in nearly equilateral triangle-shaped indent impressions with typical side lengths of $\sim 0.4 \mu\text{m}$. No cracks are observed by FE-ESEM, in good agreement with the behavior of the load-displacement curves (Figure 6A). A view of the nanoindents can be observed more closely from the AFM topography imaging owing to the higher spatial resolution of this technique. Representative 3D AFM images of the nearly regular triangle pyramid-faceted impression from the a - and c -surface exposed HA crystals are displayed in Figure 6B,C, respectively. According to the AFM observations, the probed crystals have diameters of 1.5 to 2.0 μm and lengths in the range from 10 to 15 μm . All measured HA crystals are found to be well-fixed in the calcium phosphate bone-cement matrix (see Supporting Information), since dragging of the cement-embedded particles by a Berkovich tip is not detected. In Figure 6D, the thickness profiles of the

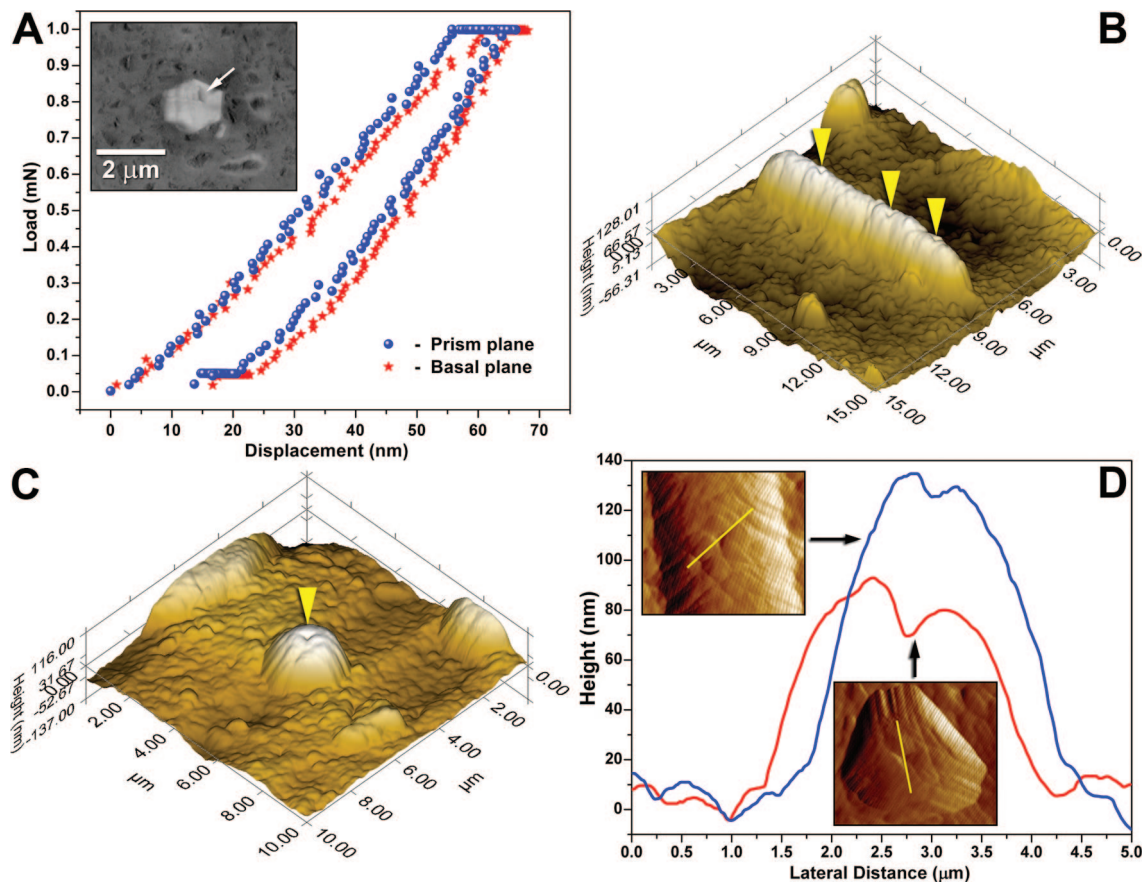


Figure 6. Representative load versus displacement curves (A) together with a 3D AFM topography view of the indentation impressions (marked by yellow arrows) acquired by NI probing on the prism-faceted (B) and basal-faceted (C) planes of the HA crystals with a well-defined hexagonal prism-like morphology. The inset in (A) is an FE-ESEM image of a specimen surface after the NI measurement, showing the nanoindent impression. Cross-section height profiles are compared in (D) with respect to the probed *a*- and *c*-surface exposed HA crystals.

nanoindenters from two different sections (marked in the respective images) are shown. These profiles reveal that both probed crystal planes exhibit a residual indentation depth of about 12–16 nm, consistent with the ones deduced from the load-displacement curves (Figure 6A). The asymmetry of these profiles at the top clearly highlights a flow of material above the edges of the nanoindenters during probing; this so-called pile-up (Figure 6D) is a characteristic feature of single-crystal particles.

Discussion

The preparation of hydroxyapatite with a different morphological shape has been the subject of many studies. In the majority of the reported approaches, phase-pure HA products are commonly characterized as either rod-like (whiskers, needles, wires, fibers, etc.)^{13,15,18} or plate-like.^{15,20,31,32} A few reports have been published where HA powders exhibit a hexagonal prism-,^{4,14,16,33} elliptical-,^{17,34} or ribbon-like³⁵ particle shape. Despite these morphological differences, the as-derived hydroxyapatite crystals typically grow along the [001] hexagonal axis, while the synthesis of differently oriented HA crystals still remains a challenge. The application for most of the cited synthesis procedures is somewhat limited however, due to the use of different additives (coordinating ligands, surfactants, etc.)^{15,16,32,34,35} or the incorporation of foreign ions into the crystal lattice of the end products.^{14,35} Additionally, most of the reported syntheses are not well developed in terms of high-yield, homogeneity of the materials properties and feasibility of large-scale production.

According to the XRD, Raman scattering and TEM, all as-synthesized samples are phase-pure hexagonal hydroxyapatite (Figures 2A, 3B, and 5). Additionally, XRD patterns reflect a textured microstructure of **PT**, **HX** and **ND**, indicating *c*-axis orientation of the crystals; this texturing trend was not observed for the **FP** product (Figure 2B). The latter observation corresponds to the overall smaller size of the **FP** crystals, as established by electron microscopy. EDX studies clearly confirm that all as-prepared samples are slightly nonstoichiometric HA, having a Ca/P molar ratio of ~ 1.75 . As established by IR spectroscopy, the observed nonstoichiometry is the result of partial substitution of the OH^- and PO_4^{3-} anions by CO_3^{2-} groups in the HA crystal structure (Figure 3A). Thus produced HA are of AB-type carbonated hydroxyapatite. This is consistent with the elemental analysis, showing ~ 0.75 wt% carbon content in the synthesized HA products. It is worth noting that biological apatite contains 3–5 wt% carbonate groups.³⁶ Hence, the as-prepared carbonated HA is the requirement rather than a problem for its biomedical application.

According to the SEM data, the particle morphology of the synthesized phase-pure HA powders is quite variable (Figure 4), depending on the applied temperature cycle and the initial concentration of the starting compounds (Table 1). When the hydrothermal synthesis is conducted at the constant temperature of 90 °C (Scheme I in Figure 1), the urea is intensively decomposed providing enhanced supersaturation, which should generate a large number of nuclei, and consequently, preferably smaller crystals should be formed. However, in our case, synthesis by Scheme I (Figure 1) yielded a highly crystalline

HA powder, which is predominantly composed of elongated, plate-like crystals with a different size on a micrometer scale (sample **PT**, Figure 4A). In general, the synthesis of hydroxyapatite proceeds through the formation of octacalcium phosphate $\text{Ca}_8\text{H}_2(\text{PO}_4)_6 \cdot 5\text{H}_2\text{O}$ (OCP), which acts as a precursor for the final HA formation.³⁶ Overall, OCP crystals are characterized by a plate-like morphology.³⁷ Therefore, it is believed that the plate-like shape and large size of **PT** crystals are due to a kinetic effect, in particular, the result of the epitaxial transformation from the intermediate OCP phase to the HA^{20,37} because of the structural similarity between both calcium orthophosphates.³⁸ The nonuniform size distribution of the as-derived **PT** plate-like crystals is presumably related to the different rate of the plate-like crystal growth during hydrothermal synthesis.

The resulting morphology of the stepwise decomposition of urea (Scheme II in Figure 1) is very different from that of kinetically determined intensive decomposition. SEM reveals that a hydrothermal synthesis by Scheme II (Figure 1) efficiently extended the overall particle morphology to a well-defined hexagonal prism-like shape, thus mimicking the crystal habit of the HA hexagonal-bipyramidal class (sample **HX**, Figure 4B). This indicates that the reaction under gentle supersaturation conditions is shifted toward the formation of a thermodynamically favorable product, thereby excluding the intensive epitaxial growth of HA from the OCP template in the form of plates. TEM, ED, and HRTEM analyses confirm that the micrometer-sized particles of **HX** are indeed HA single crystals devoid of any structural defects and oriented with their long axis along the *c*-axis (Figure 5A). The as-prepared hexagonal prism-like HA particles should possess an increased selectivity toward adsorption of negatively charged acidic proteins because of a well-developed *a*-surface (see Supporting Information, Figure S2).

SEM examination of the hydrothermally derived **ND** powder clearly demonstrates that this HA product is composed of sharply faceted microcrystals with a needle-like morphology (Figure 4C). This is consistent with the controlled slow decomposition of urea via Scheme III (Figure 1), where small numbers of nuclei are generated, resulting in a large crystal size.

Our attempts to further slow down the thermal decomposition of urea applying temperature profile of Scheme IV (Figure 1), maintaining the rest of the experimental parameters, failed. The powder XRD analysis of the as-derived product shows that such an interrupted urea decomposition pathway does not result in the formation of a significant amount of HA and OCP was obtained as the predominant phase. In the same time, a single phase HA without any admixture is formed readily with a twice lower concentration of the initial components for the hydrothermal synthesis according to Scheme IV (sample **FP**, Figure 2A). The as-derived powdered sample is composed of particles with a fine-plate-like (predominant) and rod-like appearance, as imaged by SEM (Figure 4D). In addition, the particle size of the **FP** product is much smaller than that of **PT**, **HX**, and **ND** samples.

The influence of the concentration of starting reagents on the nature of the product was further investigated. The syntheses by Schemes I, II, and III (Figure 1) using half the concentration of starting compounds lead to the single phase HA samples, exhibiting practically the same particle shape and size (not shown here) as the **FP** sample derived by Scheme IV. This highlights that the morphological characteristics of the product under certain hydrothermal conditions are primarily affected by the concentration. Hence, despite the applied temperature profile,

an effective morphology control of HA particles via governed thermal decomposition of urea is limited in the diluted precursor system.

Detailed TEM, ED, and HRTEM studies (Figure 5B,C) confirm that the particles in the **FP** sample have an hexagonal HA crystal structure. Besides the predominant formation of fine-plate-like crystals with their axis oriented along [110] (i.e., growing along the (211)), TEM indicates also the formation of rod-like particles oriented along [221], thereby growing along the (102) direction. This is somewhat surprising but an important finding of our work because HA particles exhibit a much higher tendency to grow along the *c*-axis, for example, as observed for the **HX** sample (Figure 5A). The as-synthesized differently oriented HA particles can exhibit promising selective adsorption properties.¹ ED and HRTEM also prove the single-crystalline nature and the defect-free local structure of the particles in **FP** (Figure 5B,C), demonstrating the nearly ideal fine microstructure of the HA crystals originating from the hydrothermal synthesis.

Hydroxyapatite exhibiting various morphological features is among the more promising class of compounds to reinforce the mechanical properties of bioceramics and calcium phosphate bone-cements, used in medical practice as grafts. In addition, HA based composite materials are also intensively used to mimic and investigate the mechanical behavior of the bones. Therefore, it is beneficial to study the mechanical properties of HA single crystals, which might lead to a further understanding of the mechanical behavior of the biocomposite materials. Evidently, carrying out direct measurements of the mechanical properties on HA single crystals is a nontrivial process; however, recent developments of the nanoindentation technique has enabled researchers to characterize mechanical properties at the nano level. Owing to the appropriate crystal size and shape, phase-purity, well-defined hexagonal prism-like particle morphology, single-crystalline nature and the absence of structural defects, the hydrothermally derived **HX** product has been selected to realize an NI investigation.

Both prism-faceted and basal-faceted planes representing *a*-surface and *c*-surface exposed HA crystals were probed (see Supporting Information, Figures S6A and S6B). It was established that the respective *a*- and *c*-surface of the HA single crystals exhibit a very small deformation under a constant applied load, so-called creep (Figure 6). This fact is related to a high structural regularity of HA single crystals, leading to a minimum number of slip systems. In addition, AFM observations reveal the appearance of piles-up, a typical feature of single crystals (Figure 6D). Therefore, these data together with the TEM investigation mark one of the most remarkable points of our NI experiment: the fact that we have been able to investigate mechanical properties of single crystals on a nanoscale.

It was established that the prism-faceted and basal-faceted planes possess an elastic modulus of 62 ± 7 GPa and 68 ± 8 GPa, respectively (peak load 1 mN). This NI result shows that the *c*-axis orientation is $\sim 11.5\%$ stiffer than the *a*-axis one, indicating a slight anisotropy of the HA elastic properties, most likely induced by the more close packed nature of the *c*-surfaces.³⁹ A similar anisotropic elasticity trend was also observed by Viswanath et al. in HA single crystals prepared using a molten salt synthesis,⁴⁰ and the reported differences in elasticity between basal-faceted and prism-faceted planes were $\sim 7\%$ or $\sim 27\%$, depending on the employed NI load function.⁴⁰ Nevertheless, they measured E_s values of ~ 130 GPa which are reasonably higher than that of the present **HX** hydroxyapatite crystals, but at the

same time, in good agreement with NI results on HA ceramics (~ 122 GPa).⁴¹ In contrast, Teraoka et al. reported the E_s value of ~ 64 GPa for the a -surfaces of HA crystals synthesized by the hydrothermal method at moderate temperatures (200–300 °C).⁴² This value matches well with that of the respective surface of **HX** hydroxyapatite crystals. Interestingly, the E_s values of the synthesized phase-pure HA agrees with the elastic modulus of biological hydroxyapatite from tooth enamel (~ 60 GPa).⁴³ Therefore, it appears that the observed difference in E_s values is induced by the influence of the preparation technique on the elastic modulus. In terms of synthesis, HA crystals and ceramic were generated by a molten salt method and sintering, respectively ($T > 1000$ °C).^{40,41} Owing to the annealing of the lattice impurities and defects, such high-temperature synthesis procedures lead to the formation of HA products structurally very close to the ideal hydroxyapatite. Thereby, high E_s values were observed, which almost attain the E_s value calculated for the basal-faceted plane of a HA single crystal (~ 138 GPa).⁴⁴

NI probing reveals that the prism-faceted and basal-faceted planes of single-crystalline HA with an hexagonal prism-like particle morphology exhibit a hardness of 5.9 ± 0.8 GPa and 5.7 ± 0.9 GPa, respectively (peak load 1 mN). However, in contrast to the published data,⁴⁰ these two values are found to be alike within one standard deviation. The lack of difference between H values for a - and c -surfaces most likely stem from technical limitations. Specifically, the crystal surface appears to be not flat enough at a nanoscale (Figure 6B–D), while performing measurements using a peak load of 1 mN generates indentation depths on the order of nanometers. Consequently, estimating the contact area from the contact depth can lead to significant errors when the surface exhibits such an uneven surface at the nanoscale. Hence, a difference of hardness from the prism-faceted and basal-faceted planes of the **HX** crystals cannot be excluded. A further study is currently underway to try to overcome this experimental obstacle.

Conclusions

Hydroxyapatite powdered samples were successfully synthesized on a gram scale through a urea-assisted hydrothermal reaction between $\text{Ca}(\text{NO}_3)_2 \cdot 4\text{H}_2\text{O}$ and $(\text{NH}_4)_2\text{HPO}_4$ at a low temperature of 90 °C. The particle morphology of the HA crystals can easily be controlled by judiciously varying the decomposition kinetics of urea and the concentration of the initial components in the course of the hydrothermal process. Detailed experimental studies clearly demonstrate that the as-derived products are composed of single-crystalline, structural defect-free, carbonated hydroxyapatite crystals, exhibiting a plate-like, hexagonal prism-like, needle-like and fine-plate-like particle morphology. Furthermore, we have been able to probe the mechanical properties of HA single crystals by nanoindentation, and the obtained data conclusively highlight that the hardness and elastic modulus are determined by the crystal orientation and the synthesis route.

Acknowledgment. The authors are grateful to Dr. K. A. Kovnir for the fruitful discussion. This work was partially supported by the Spanish Ministry of Education and Science (MAT2002-03857), the European Union Marie Curie EST Fellowship on Biomimetic Systems (MEST-CT-2004-504465), and the European Union Framework 6 Program under a contract for an Integrated Infrastructure Initiative (Reference [026019] ESTEEM).

Supporting Information Available: The text document containing the NI measurement details (pages SI2–SI3). Representations, illustrating hexagonal crystal structure view along [001] and the surface charging of HA (Figures S1 and S2). Images, giving a general overview of the hydrothermal setup and hydrothermally derived products (Figures S3 and S4). Representation and FE-ESEM images showing the cement-embedded HA particles for NI (Figures S5 and S6). This material is available free of charge via the Internet at <http://pubs.acs.org>.

References

- (1) Kawasaki, T. Hydroxyapatite as a liquid chromatographic packing. *J. Chromatogr.* **1991**, *544* (1–2), 147–184.
- (2) LeGeros, R. Z. Properties of osteoconductive biomaterials: calcium phosphates. *Clin. Orthop. Relat. Res.* **2002**, *395* (Feb.), 81–98.
- (3) Kawachi, G.; Sasaki, S.; Nakahara, K.; Ishida, E. H.; Ioku, K. Porous apatite carrier prepared by hydrothermal method. *Key Eng. Mater.* **2006**, *309–311*, 935–938.
- (4) Vasiliev, A. N.; Zlotnikov, E.; Khinast, J. G.; Riman, R. E. Chemisorption of silane compounds on hydroxyapatites of various morphologies. *Scr. Mater.* **2008**, *58* (12), 1039–1042.
- (5) Lakes, R. S. Composite biomaterials. In *Biomaterials. Principles and Applications*, 2nd ed.; Park, J. B.; Bronzino, J. D., Eds.; CRC Press: Boca Raton, FL, 2003; pp 79–93.
- (6) Müller, F. A.; Gbureck, U.; Kasuga, T.; Mizutani, Y.; Barralet, J. E. Whisker-reinforced calcium phosphate cements. *J. Am. Ceram. Soc.* **2007**, *90* (11), 3694–3697.
- (7) Roeder, R. K.; Sproul, M. M.; Turner, C. H. Hydroxyapatite whiskers provide improved mechanical properties in reinforced polymer composites. *J. Biomed. Mater. Res.* **2003**, *67A* (3), 801–812.
- (8) Posner, A. S. The mineral of bone. *Clin. Orthop. Relat. Res.* **1985**, *200* (Nov.), 87–99.
- (9) Cuisinier, F.; Robinson, C. The structure of teeth: human enamel crystal structure. In *Handbook of Biomineralization. Medical and Clinical Aspects*; Epple, M.; Baeuerlein, E., Eds.; Wiley-VCH: Weinheim, 2007; pp 177–182.
- (10) Russell, R. G. G.; Caswell, A. M.; Hearn, P. R.; Sharrard, R. M. Calcium in mineralized tissues and pathological calcification. *Brit. Med. Bull.* **1986**, *42* (4), 435–446.
- (11) Péru, L.; Daculsi, G. Synthetic calcium phosphates: models for biological crystals. *Clin. Mater.* **1994**, *15* (4), 267–272.
- (12) Ito, A.; Onuma, K., Growth of hydroxyapatite crystals. In *Crystal Growth Technology*; Byrappa, K.; Ohachi, T., Eds.; Springer-Verlag: Berlin, 2003; pp 525–548.
- (13) Tanahashi, M.; Kamiya, K.; Suzuki, T.; Nasu, H. Fibrous hydroxyapatite grown in the gel system: effects of pH of the solution on the growth rate and morphology. *J. Mater. Sci. Mater. Med.* **1992**, *3* (1), 48–53.
- (14) Taş, A. C. Molten salt synthesis of calcium hydroxyapatite whiskers. *J. Am. Ceram. Soc.* **2001**, *84* (2), 295–300.
- (15) Wang, X.; Zhuang, J.; Peng, Q.; Li, Y. Liquid-solid-solution synthesis of biomedical hydroxyapatite nanorods. *Adv. Mater.* **2006**, *18* (15), 2031–2034.
- (16) Wei, M.; Wang, X.-X. Ribbon-like and rod-like hydroxyapatite crystals deposited on titanium surface with electrochemical method. *Mater. Lett.* **2007**, *61* (19–20), 4062–4065.
- (17) Park, H. C.; Baek, D. J.; M, P. Y.; Yoon, S. Y. Thermal stability of hydroxyapatite whiskers derived from the hydrolysis of α -TCP. *J. Mater. Sci.* **2004**, *39* (7), 2531–2534.
- (18) Suchanek, W.; Yoshimura, M. Processing and properties of hydroxyapatite-based biomaterials for use as hard tissue replacement implants. *J. Mater. Res.* **1998**, *13* (1), 94–117.
- (19) Byrappa, K.; Yoshimura, M., *Handbook of Hydrothermal Technology. A Technology for Crystal Growth and Materials Processing*; Noyes Publications: New Jersey, 2001; p 53.
- (20) Neira, I. S.; Guitián, F.; Taniguchi, T.; Watanabe, T.; Yoshimura, M. Hydrothermal synthesis of hydroxyapatite whiskers with sharp faceted hexagonal morphology. *J. Mater. Sci.* **2008**, *43* (7), 2171–2178.
- (21) *Phase Diagrams for Ceramists*; Levin, E. M.; Robbins, C. R.; McMurdie, H. F., Eds.; American Ceramic Society: Columbus, OH, 1964; Vol. I, Diag. 246.
- (22) Kolen'ko, Yu. V.; Kovnir, K. A.; Neira, I. S.; Taniguchi, T.; Ishigaki, T.; Watanabe, T.; Sakamoto, N.; Yoshimura, M. A novel, controlled and high-yield solvothermal drying route to nanosized barium titanate powders. *J. Phys. Chem. C* **2007**, *111* (20), 7306–7318.
- (23) Willard, H. H.; Tang, N. K. A study of the precipitation of aluminum basic sulfate by urea. *J. Am. Chem. Soc.* **1937**, *59* (7), 1190–1196.

- (24) Oliver, W. C.; Pharr, G. M. An improved technique for determining hardness and elastic-modulus using load and displacement sensing indentation experiments. *J. Mater. Res.* **1992**, *7* (6), 1564–1583.
- (25) Turner, C. H.; Burr, D. B., Experimental techniques for bone mechanics. In *Bone Mechanics Handbook*, 2nd ed.; Cowin, S. C., Ed.; CPC Press: Boca Raton, FL, 2001; pp 7–20.
- (26) Grenoble, D. E.; Katz, J. L.; Dunn, K. L.; Gilmore, R. S.; Murty, K. L. The elastic properties of hard tissues and apatites. *J. Biomed. Mater. Res.* **1972**, (6), 3.
- (27) Koutsopoulos, S. Synthesis and characterization of hydroxyapatite crystals. A review study on the analytical methods. *J. Biomed. Mater. Res.* **2002**, *62* (4), 600–612.
- (28) Nakamoto, K. *Infrared and Raman Spectra of Inorganic and Coordination Compounds, Part B: Applications in Coordination, Organometallic and Bioinorganic Chemistry*, 5th ed.; John Wiley & Sons Inc: New York, 1997; pp 54–148.
- (29) Monma, H.; Takahashi, T. Preparation and thermal changes of carbonate-containing apatite. *Gypsum Lime* **1987**, *210*, 287–291.
- (30) Li, X.; Bhushan, B. A review of nanoindentation continuous stiffness measurement technique and its applications. *Mater. Charact.* **2002**, *48* (1), 11–36.
- (31) Loo, S. C. J.; Siew, Y. E.; Ho, S.; Boey, F. Y. C.; Ma, J. Synthesis and hydrothermal treatment of nanostructured hydroxyapatite of controllable sizes. *J. Mater. Sci. Mater. Med.* **2008**, *19* (3), 1389–1397.
- (32) Nagata, F.; Toriyama, M.; Teraoka, K.; Yokogawa, Y. Influence of ethylamine on the crystal growth of hydroxyapatite crystals. *Chem. Lett.* **2001**, *30* (8), 780–781.
- (33) Ashok, M.; Narayana Kalkura, S.; Meenakshi Sundaram, N.; Arivuoli, D. Growth and characterization of hydroxyapatite crystals by hydrothermal method. *J. Mater. Sci. Mater. Med.* **2007**, *18* (15), 895–898.
- (34) Zhou, Z.-H.; Zhou, P.-L.; Yang, S.-P.; Yu, X.-B.; Yang, L.-Z. Controllable synthesis of hydroxyapatite nanocrystals via a dendrimer-assisted hydrothermal process. *Mater. Res. Bull.* **2007**, *42* (9), 1611–1618.
- (35) Zhang, H. G.; Zhu, Q.; Wang, Y. Morphologically controlled synthesis of hydroxyapatite with partial substitution of fluorine. *Chem. Mater.* **2005**, *17* (23), 5824–5830.
- (36) Elliott, J. C. *Structure and Chemistry of the Apatites and Other Calcium Orthophosphates*, 1st ed.; Elsevier: Amsterdam, 1994; pp 12, 259.
- (37) Nancollas, G. H. Phase transformation during precipitation of calcium salts. In *Biological Mineralization and Demineralization*; Nancollas, G. H., Ed.; Springer-Verlag: Heidelberg, 1982; pp 79–99.
- (38) Brown, W. E. Octacalcium phosphate and hydroxyapatite: crystal structure of octacalcium. *Nature* **1962**, *196* (4859), 1048–1049.
- (39) Kay, M. I.; Young, R. A.; Posner, A. S. Crystal structure of hydroxyapatite. *Nature* **1964**, *204* (4963), 1050–1053.
- (40) Viswanath, B.; Raghavan, R.; Ramamurty, U.; Ravishankar, N. Mechanical properties and anisotropy in hydroxyapatite single crystals. *Scr. Mater.* **2007**, *57*, 361–364.
- (41) Kumar, R. R.; Wang, M. Modulus and hardness evaluations of sintered bioceramic powders and functionally graded bioactive composites by nano-indentation technique. *Mater. Sci. Eng., A* **2002**, *338*, 230–236.
- (42) Teraoka, K.; Ito, A.; Maekawa, K.; Onuma, K.; Tateishi, T.; Tsutsumi, S. Mechanical properties of hydroxyapatite and OH-carbonates hydroxyapatite single crystals. *J. Dent. Res.* **1998**, *77* (7), 1560–1568.
- (43) Imbeni, V.; Kruzic, J. J.; Marshall, G. W.; Marshall, S. J.; Ritchie, R. O. The dentin-enamel junction and the fracture of human teeth. *Nat. Mater.* **2005**, *4* (3), 229–232.
- (44) Katz, J. L.; Ukraincik, K. On the anisotropic elastic properties of hydroxyapatite. *J. Biomech.* **1971**, *4* (3), 221–227.

CG800738A